Controlling Plasmon-Enhanced Fluorescence via Intersystem Crossing in Photoswitchable Molecules

Mingsong Wang, Gregory Hartmann, Zilong Wu, Leonardo Scarabelli, Bharath Bangalore Rajeeva, Jeremy W. Jarrett, Evan P. Perillo, Andrew K. Dunn, Luis M. Liz-Marzán, Gyeong S. Hwang, Yuebing Zheng

M. Wang, Z. Wu, B. Bangalore Rajeeva, Prof. Dr. Y. Zheng
Department of Mechanical Engineering
Texas Materials Institute
The University of Texas at Austin
Austin, TX 78712, USA
E-mail: zheng@austin.utexas.edu (Y. B. Z.)
G. Hartmann, Prof. Dr. G. S. Hwang
Department of Chemical Engineering
The University of Texas at Austin
Austin, TX 78712, USA
Dr. L. Scarabelli, Prof. Dr. L. M. Liz-Marzán
Bionanoplasmonics Laboratory
CIC biomaGUNE
Paseo de Miramón 182, 20014 Donostia-San Sebastián, Spain
Dr. L. Scarabell
Department of Chemistry and Biochemistry,
California NanoSystems Institute,
University of California, Los Angeles,
Los Angeles, California 90095, USA
Prof. Dr. L. M. Liz-Marzán
Ikerbasque, Basque Foundation for Science
48013 Bilbao, Spain
Prof. Dr. L. M. Liz-Marzán
Biomedical Research Networking Center in Bioengineering, Biomaterials, and Nanomedicine
CIBER-BBN, 20014 Donostia- San Sebastián, Spain
Dr. J. W. Jarrett, E. P. Perillo, Prof. Dr. A. K. Dunn
Department of Biomedical Engineering,
The University of Texas at Austin
Austin, TX 78712, USA

By harnessing photoswitchable intersystem crossing (ISC) in spiropyran (SP) molecules,

active control of plasmon-enhanced fluorescence in the hybrid systems of SP molecules and

plasmonic nanostructures is achieved. Specifically, SP-derived merocyanine (MC) molecules formed by photochemical ring-opening reaction display efficient ISC due to their zwitterionic character. In contrast, ISC in quinoidal MC molecules formed by thermal ring-opening reaction is negligible. The high ISC rate can improve fluorescence quantum yield (QY) of the plasmon-modified spontaneous emission, only when the plasmonic electromagnetic field enhancement is sufficiently high. Along this line, we demonstrate extensive photo-modulation of fluorescence by switching the ISC in MC molecules at Au nanoparticle aggregates, where strongly enhanced plasmonic hot spots exist. The ISC-mediated plasmon-enhanced fluorescence represents a new approach toward controlling the spontaneous emission of fluorophores near plasmonic nanostructures, which will expland the applications of active molecular plasmonics in information processing, biosensing and bioimaging.

1. Introduction

Controlling the spontaneous emission of fluorophores at the nanoscale is critical to the development of nano-lasers, single-photon sources and high-resolution fluorescence biomarkers, for applications in information processing, biosensing and bioimaging.[1-7] Modification of spontaneous emission of a fluorophore was reported decades ago.[8] Since then, tremendous development of nanophotonic technology has enabled exploring the control over the spontaneous emission of fluorophores at the nanoscale and below.[1, 5-6, 9-15] Among many nanophotonic systems, plasmonic nanostructures present multiple advantages for controlling fluorescence, including: (1) strong electromagnetic field (E-field) enhancement upon excitation of surface plasmons; (2) small size of plasmonic nanostructures for device miniaturization; (3) highly confined "hot spots", relevant to single fluorophores in size; and (4) high chemical stability of noble metals in plasmonic nanostructures.[16-25]

Extensive studies on plasmon-enhanced fluorescence have focused on applying plasmonic nanostructures with large field enhancement and low optical loss to increase the excitation

and radiative-decay rates of fluorophores. However, the fluorescence QY is also influenced by non-radiative decay rates that can be increased by the plasmon-induced high electromagnetic fields. The non-radiative decay channels vary in different molecular systems. In the presence of a strong spin-orbit coupling, an additional decay channel occurs when the first excited singlet state transfers to the triplet state, a process known as intersystem crossing (ISC). So far, most of the studies on plasmon-enhanced fluorescence have ignored the possible influence of ISC.[3, 9, 11-13, 22, 26-29] However, for some dye molecules such as spiropyran (SP)-derived merocyanine (MC) molecules, ISC can be an efficient non-radiative decay pathway of the first excited singlet state.[30-31] Therefore, understanding and controlling the effects of ISC on plasmon-enhanced fluorescence may advance both fundamental research and applications.

Herein, we explore and exploit the intrinsic ISC of photochromic molecules to control their plasmon-enhanced fluorescence. Specifically, we used hybrid systems comprising photochromic SP molecules and a single plasmonic nanoparticle (NP) or NP aggregates, as platforms to demonstrate that (1) ISC-mediated plasmon-enhanced fluorescence of photoswitchabe molecules leads to a large modulation of light emission from the hybrid systems, and (2) as a non-radiative decay pathway, counterintuitively, ISC can improve the plasmonic enhancement of the fluorescence of molecules when there is strong electromagnetic field enhancement and the ISC rate is sufficiently fast.

It has been known that SP molecules can convert to MC via either photochemical ring-opening or thermal ring-opening reactions.[32-33] Photochemical ring-opening reactions proceed through a heterolytic C-O bond cleavage, producing the zwitterionic MC form. Thermal ring-opening reactions follow a 6p electro-cyclic ring opening, producing the quinoidal MC form, (**Figure 1**a). A zwitterionic character in the singlet wave function, which contains a positive and a negative charge, is favorable for ISC.[34-36] While the zwitterionic MC form has efficient ISC,[30-31] the quinoidal MC form lacks the zwitterionic character and

4

thus the ISC. Therefore, the decay channels of the first excited singlet state are different in the zwitterionic and the quinoidal MC forms, as indicated in Figure 1b. Thus, the fluorescence QY of zwitterionic MC molecules (ϕ_0) and quinoidal MC molecules (ϕ_0'), without plasmonic nanostructures, can be expressed as[9, 13, 26]:

$$\phi_0 = \frac{\gamma_r}{\gamma_r + \gamma_{nr} + \gamma_{ISC}} , \qquad (1)$$

and

$$\phi_0' = \frac{\gamma_r'}{\gamma_r' + \gamma_{nr}'} , \qquad (2)$$

where γ_r, γ_{nr} and γ_{ISC} represent the radiative decay rate, non-radiative (excluding ISC) decay rate, and ISC rate of zwitterionic MC molecules, respectively. γ_r' and γ_{nr}' are the radiative and non-radiative decay rates of quinoidal MC molecules, respectively. We use (´) to distinguish the parameters of the quinoidal MC molecule from those of the zwitterionic MC molecule.
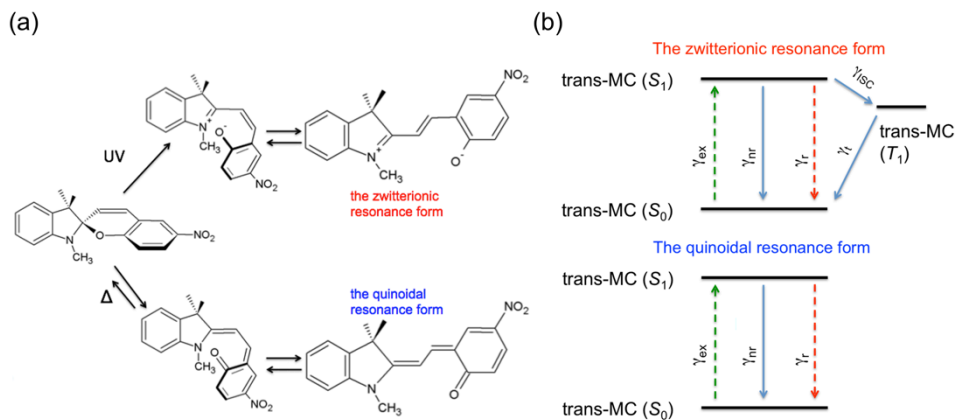

Figure 1. a) Schematic representation of the photochemical (up pathway) and thermal (down pathway) ring-opening reactions of SP molecules. b) Jablonski diagram with the relevant energy states for both forms. γ_{ex} is the excitation rate, γ_r is the radiative decay rate, γ_{nr} is the non-radiative decay rate, γ_{ISC} is the rate of intersystem crossing, and γ_t is the triplet decay rate.

2. Results and Discussion

Our samples were prepared by drop-casting Au nanospheres (AuNSs) and Au nanotriangles (AuNTs) on glass slides,[37] followed by spin-coating of SP-doped PMMA films

to cover the AuNSs and AuNTs, as shown in **Figure 2**a (a more detailed description can be found in the Experimental Section). The photoisomerization of SP in the PMMA matrix was confirmed by FTIR and UV-vis absorption spectra under different light irradiation (see **Figure S1**, Supporting Information). Upon white light excitation of the molecules, photoswitchable fluorescence can be observed in a dark-field optical microscope after alternating UV and green light irradiation, as shown in Figure 2b.[38] The fluorescence of zwitterionic MC molecules, which are formed via photochemical ring opening reaction upon UV irradiation, features an emission band centered at 670 nm (Figure 2b, purple line), which is in good agreement with the fluorescence measured in a conventional fluorometer.[39-41] The zwitterionic MC molecules are stable in the PMMA matrix due to the increased polarity of their microenvironment.[42-45] This increased polarity arises from the formation of a large number of zwitterionic MC molecules in the PMMA matrix during UV irradiation. Both the as-prepared sample and the sample after green irradiation feature emission bands centered at ~650 nm (Figure 2b, red and green lines). The emission cannot be attributed to SP molecules, which were reported to have an emission band centered around ~530 nm under UV light excitation (our white halogen light source does not contain UV light, see spectrum in **Figure S2**, Supporting Information).[32] We attribute the ~650 nm emission to the quinoidal MC molecules, which are formed through a thermal ring-opening reaction (see **Figure S3** and detailed discussion in Supporting Information).[32] The thermal ring-opening reaction occurs in our experiments due to temperature increase (see detailed information in the Experimental Section) at the optically irradiated spots. Therefore, our molecular system combined with plasmonic nanoparticles provides an ideal platform to investigate how the intrinsic ISC affects plasmon-enhanced fluorescence,
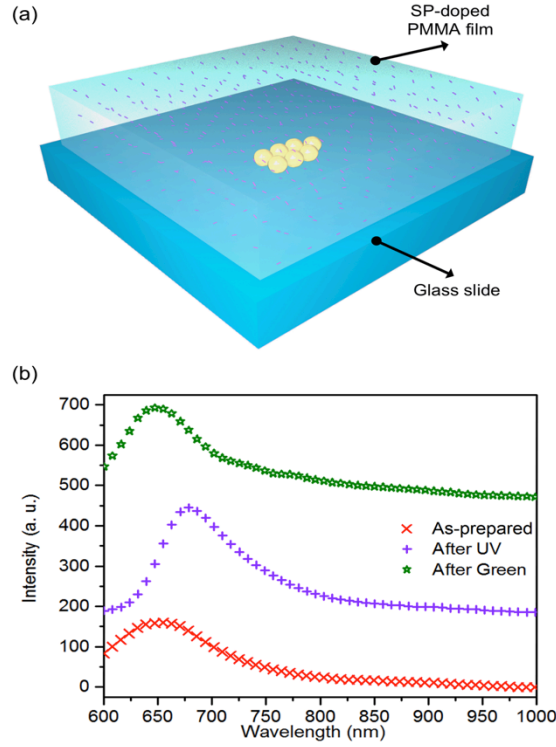
Figure 2. a) Schematic view of a sample comprising a single AuNS aggregate on a glass substrate, covered by an SP-doped PMMA thin film. b) Photoswitchable fluorescence of pure photochromic molecules. Specifically, the curve made of red crosses represents the molecular fluorescence before irradiation on the sample. The curves made of purple and green symbols represent molecular fluorescence after UV and green light irradiation on the sample, respectively. An intensity-axis offset was added for clarity.

The fluorescence of a molecular emitter is enhanced when the molecule is near a plasmonic nanostructure that exhibits a localized surface plasmon resonance (LSPR) at a wavelength matching the fluorescence peak of the emitter.[9, 46] The radiative decay rate enhancement is calculated by:[9, 46]

$$\frac{\gamma_r}{\gamma_{r0}} = \left| \mathbf{n}_p + k^2 \frac{1}{\varepsilon_0} \overleftrightarrow{\alpha}(\omega) \overleftrightarrow{G}(\mathbf{r}_p, \mathbf{r}_0; \omega) \mathbf{n}_p \right|^2, \tag{3}$$

where γ_r is the radiative decay rate in the presence of the plasmonic nanostructure, γ_{r0} is the radiative decay rate without the plasmonic nanostructure, $\mathbf{n}_p$ is the unit vector in the direction of the molecule's dipole moment, k is the wavevector of emitted light, ω is frequency of emitted light, $\overleftrightarrow{\alpha}$ is the particle's polarizability, $\overleftrightarrow{G}$ is the system's dyadic Green's function, $\mathbf{r}_0$ is the position vector of the molecules, and $\mathbf{r}_p$ is the position vector of the particles.

The enhanced E-field by the plasmonic nanostructure, $\mathbf{E}_p(\mathbf{r}_0)$, equals:[46]

$$\mathbf{E}_p(\mathbf{r}_0) = k^2 \frac{1}{\varepsilon_0} \overleftrightarrow{\alpha}(\omega)\overleftrightarrow{G}(\mathbf{r}_p, \mathbf{r}_0; \omega)\mathbf{E}_0(\mathbf{r}_p), \qquad (4)$$

where $\mathbf{E}_0(\mathbf{r}_p)$ is the E-field of the incident light. By combining equations 3 and 4, we obtain:

$$\frac{\gamma_r}{\gamma_{r0}} = \left| \mathbf{n}_p + \frac{\mathbf{E}_p(\mathbf{r}_0)}{\mathbf{E}_0(\mathbf{r}_p)}\mathbf{n}_p \right|^2. \qquad (5)$$

From equation 5, it is clear that a larger E-field enhancement leads to a larger radiative decay rate enhancement, and when $\mathbf{E}_p(\mathbf{r}_0)$ is much larger than $\mathbf{E}_0(\mathbf{r}_p)$ approximately $\frac{\gamma_r}{\gamma_{r0}} \propto \left|\mathbf{E}_p(\mathbf{r}_0)\right|^2$.

Since both plasmonic NP aggregates with small inter-particle gaps and NPs with sharp tips can lead to a large E-field enhancement,[37, 47-50] we selected for our experiments self-assembled gold nanosphere (AuNS) aggregates with small inter-particle gaps and single gold nanotriangles (AuNTs) featuring sharp tips. Self-assembly is chosen to obtain AuNS aggregates with small inter-particle gaps, which are difficult to be obtained by other methods, such as the electron-beam lithography. In the former case we use AuNSs with a diameter of 60 nm (see SEM image of AuNSs in **Figure S4**a, Supporting Information). AuNTs have an average edge length of 60 nm and an average thickness of 30 nm (see TEM image in Figure S4b, Supporting Information). Most importantly, both systems were carefully chosen to have an optical scattering peak at ~700 nm (when covered with PMMA films or SP-doped PMMA films) that can match the fluorescence rather than the absorption of MC molecules (**Figure 3**a and **3b**). This peak wavelength can avoid the influence from the fluorescence enhancement by the plasmon-induced excitation enhancement and resonance energy transfer.[10, 38] Moreover, this particular aggregate was selected because it shows the largest fluorescence enhancement during repeated measurements. It is also worth mentioning that, the energy bandgap of ISC is smaller than that of the molecule's emission, as shown in Figure 1b. Since the LSPR bands of AuNS aggregates and AuNTs match the emission band of the molecules, there is also a

mismatch between the energy bands of LSPRs and ISC. Therefore, the influence from LSPRs on the ISC process is weak.
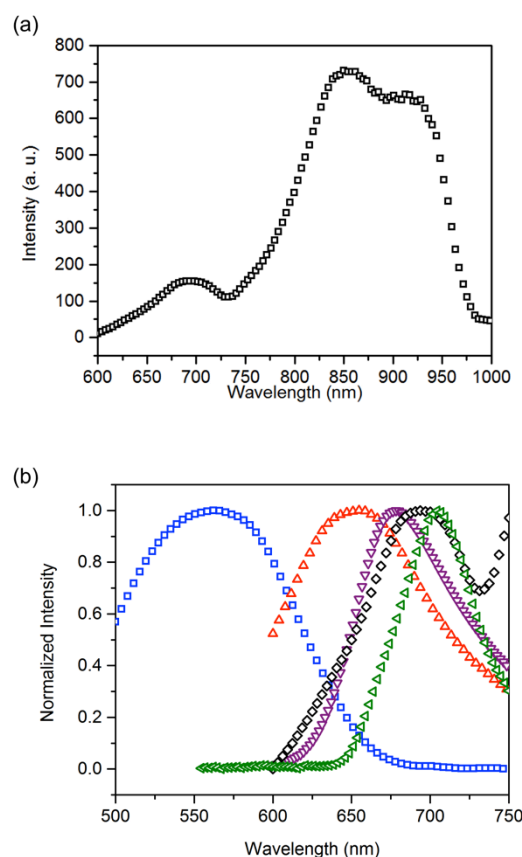
Figure 3. a) Scattering spectrum of an AuNS aggregate covered with a pure PMMA film. b) Normalized scattering spectra of the AuNS aggregate (black diamonds) and a single AuNT (green triangles); fluorescence spectra of the as-prepared sample (red triangles) and the sample after UV irradiation (purple triangles); and absorption spectrum of the sample after UV irradiation (blue squares). The cutoff of some of the spectra in b) is due to the limited working range of the grating in our spectrometer.

The dark-field scattering spectrum of the AuNS aggregate in Figure 3a (see the SEM image in the inset of **Figure 4**a) displays three scattering peaks. In order to identify the plasmonic mode of each peak, we conducted FDTD calculations to simulate the scattering spectrum of an AuNS aggregate covered by PMMA, as shown in Figure 4. The E-field distribution of the simulated scattering peak at 700 nm (Figure 4c) indicates that the experimentally measured scattering peak at 695 nm is derived from the gap plasmon mode between two nearby AuNSs along the y axis. It can also be seen that the scattering peaks at 630 nm, 854 nm and 915 nm arise from the plasmon gap mode along the x axis, the near-field

coupling between two AuNSs along the *x* axis, and the near-field coupling among three

AuNSs along the *y* axis, respectively. Figure 4b shows the simulated scattering spectrum of

the AuNT when the polarization of the incident light is along one side of the AuNT. The

scattering peak wavelength matches well our experimental spectrum (green triangles curve in

Figure 3b and scattering spectra in **Figure S5**), which arises from the plasmon dipole mode.

Figures 4e and 4f illustrate the absolute E-field distributions of the AuNS aggregate and the

AuNT, respectively. From the absolute E-field distributions, we know the E-field

enhancement near the AuNS aggregate is 50-60 times larger than that near the single AuNT.
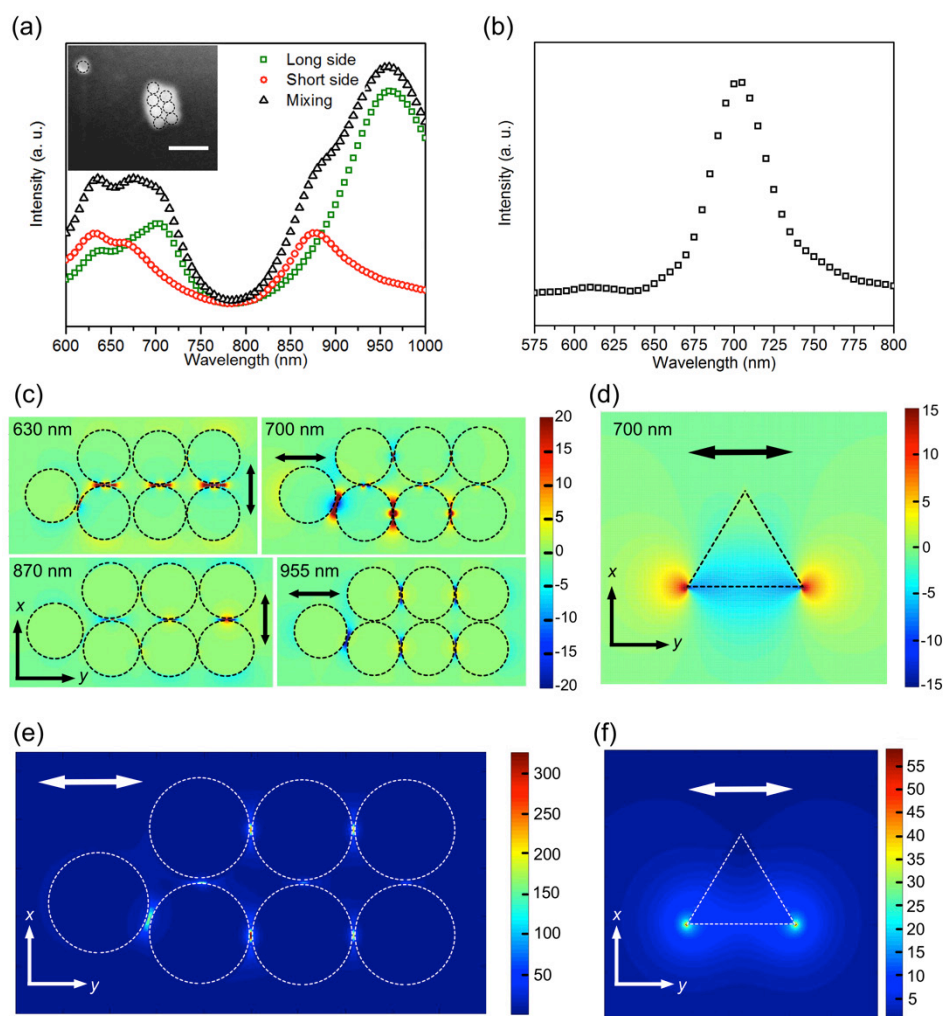
Figure 4. a) Simulated scattering spectra of an AuNS aggregate under different polarizations of incident light. SEM image in inset shows an AuNS aggregate and a single AuNS. The dashed circles indicate the AuNSs. b) Simulated scattering spectrum of a single AuNT. c) *x* components and *y* components of E-field distributions, which indicate gap dipole modes of the AuNS aggregate at 630 nm and 700 nm, and dipole modes of the AuNS aggregate at 870

nm and 955 nm. d) E-field distribution of the dipole mode of the AuNT at 700 nm e) Absolute E-field distribution of the AuNS aggregate at 700 nm f) Absolute E-field distribution of the AuNT at 700 nm. The double-headed arrows show the polarization of the incident light.

The broad absorption spectrum (blue square) in Figure 3b is likely attributed to different strereoisomers of *trans*-MC (**Figure S6**, Supporting Information), which were created by UV irradiation. As presented in **Table S1** (Supporting Information), there is a small energy difference (< 0.1 eV) between the stereoisomers, and their absorption peak wavelengths (λ_{max}), varying by 20-25 nm depending on the exchange-correlation function employed in density functional theory (DFT) calculations. We also considered the possibility that MC molecules may exist in both non-polar quinoidal and dipolar zwitterionic states, depending on the polarization of the local environment. However, the influence of polarization on λ_{max} (e.g., $\Delta\lambda_{max}\approx10$ nm, when the dielectric constant changes from 4 to 78.4, as shown in Table S3, Supporting Information) is found to be not as significant as that of isomerization; this implies that the absorption spectra due to the quinoidal and zwitterionic MC forms, even if they coexist in our samples, would be hard to distinguish.

Figure 5a illustrates the large photoswitchable fluorescence from SP molecules near an AuNS aggregate. After UV irradiation, the emission peak at 675 nm matches the fluorescence peak of zwitterionic MC (purple curve in Figure 3b) and has a higher intensity than that of the zwitterionic MC and the scattering peak of the AuNS aggregate at 695 nm (Figure 3a). The integrated intensity of the enhanced fluorescence from the hybrid is approximately 32 times that of pure MC molecules. To avoid interference with scattering peaks at longer wavelengths (Figure 3a), the integration is limited to a wavelength range from 600 to 725 nm. In contrast, the integrated intensity of the fluorescence (with removal of pure scattering by the AuNS aggregate) from the hybrid after green light radiation, is only 1.3 times that of pure MC molecules (Figure 5b, curve of green squares). Therefore, no obvious fluorescence enhancement or quenching are observed for the quinoidal MC form. The fluorescence

enhancements obtained from the molecules near 5 different AuNS aggregates that exhibit

LSPR bands overlapping the fluorescence band of MC molecules are listed in Table 1. Not all

AuNS aggregates lead to an equally large fluorescence enhancement. The enhancement

differences cannot be attributed to the relative orientation of molecules with respect to AuNS

aggregates because there are a large number of randomly oriented molecules near the AuNS

aggregates; however, it may arise from the difference in the total number of molecules at

plasmonic hot spots, since the number and size of hot spots vary for different AuNS

aggregates.
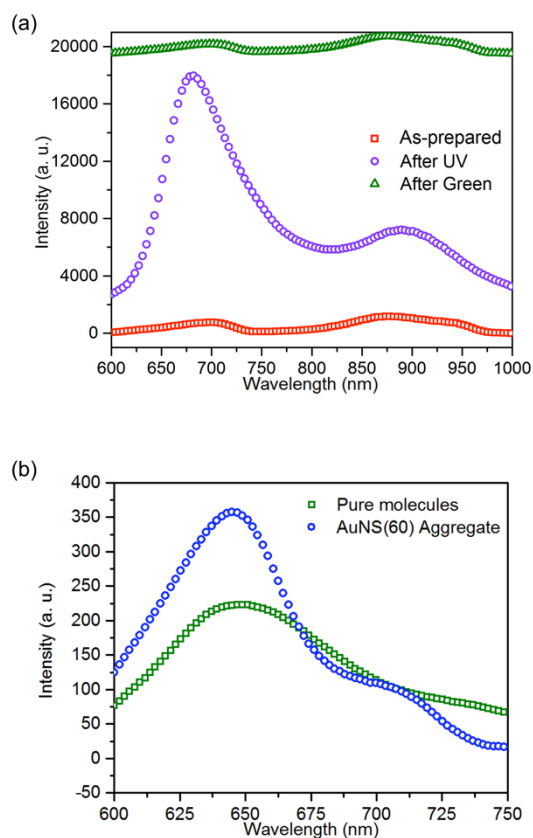
Figure 5. a) Large photoswitchable fluorescence enhancement from a hybrid containing MC molecules and an AuNS aggregate. The intensity-axis offset is added for clarity. b) Fluorescence spectra measured near and far away from the AuNS aggregate covered by the SP-doped PMMA film after green light irradiation. The fluorescence spectrum of molecules near the AuNS aggregate is obtained by removing the scattering by the AuNS aggregate.

Table 1. Comparison between the fluorescence enhancements near single AuNS aggregates and single AuNTs.

Single AuNS	Enhancement rate	Single AuNT	Enhancement rate

aggregate			
Aggregate 1	31.7	AuNT 1	1.3
Aggregate 2	15.4	AuNT 2	1.6
Aggregate 3	3.9	AuNT 3	1.1
Aggregate 4	7.5	AuNT 4	0.8
Aggregate 5	3.3	AuNT 5	1.3

For the sample consisting of AuNTs covered by a molecule-doped PMMA film, two peaks appear in the dark-field optical spectra of a single AuNT (**Figure 6**a). By removing the scattering signal from the pure AuNT (Figure 6b), we obtain the fluorescence signals from the molecules near the AuNT (Figure 6c). No obvious fluorescence enhancement is observed for the molecules near the AuNT when compared to the molecules without the AuNT in Figure 5d. The fluorescence enhancement factors for the molecules near 5 different AuNTs are listed in Table 1. All the enhancement factors are close to 1.
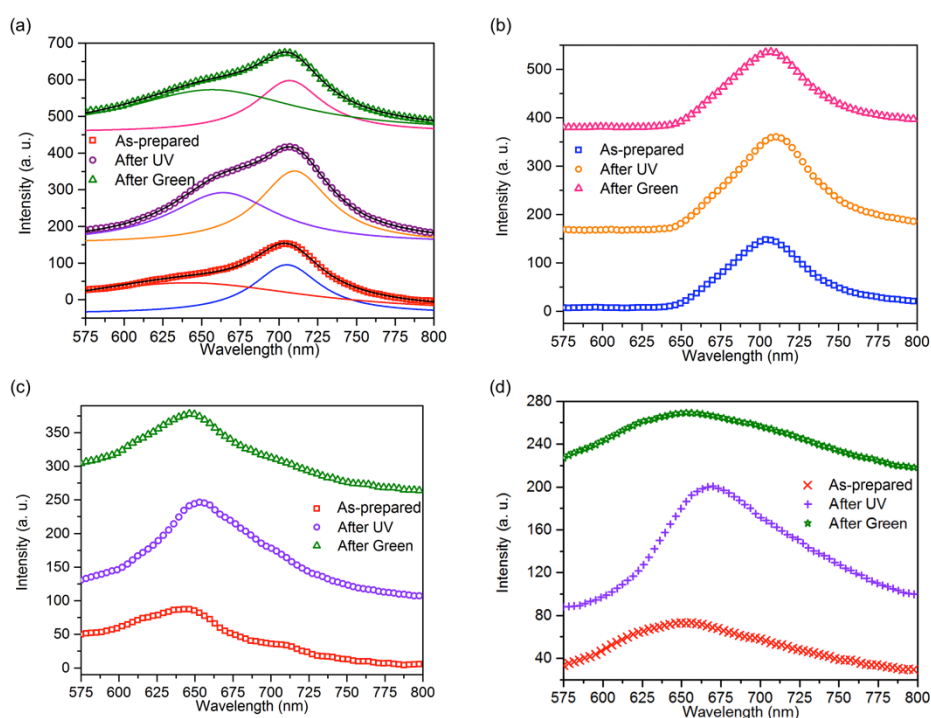
Figure 6. a) Dark-field optical spectra of a single AuNT covered by an SP-doped PMMA film under different light irradiation. The solid lines were obtained by fitting the dark-field spectra into two Lorentzian peaks. The peak wavelengths of the fitted blue, orange and pink solid lines match those in the scattering spectra in b). The peak wavelengths of red, purple and green solid lines are close to the fluorescence peak wavelengths of the pure molecules as shown in d). b) Scattering spectra of the same single AuNT as in a), under different light irradiation. The scattering spectra were obtained by blocking the fluorescence of molecules

with a 665 long pass filter, because the absorption peak of zwitterionic MC molecules is at 560 nm (Figure 3b). The slight redshift of the scattering peak after UV irradiation can be explained by a change in the refractive index around the AuNT since zwitterionic MC molecules have a larger refractive index than SP molecules. c) Fluorescence spectra of molecules near the same AuNT as in a) under different light irradiation. These spectra were acquired by subtracting the scattering spectra in b) from the dark-field spectra in a). d) Fluorescence spectra of molecules away from AuNTs under different light irradiation in the same sample. The intensity-axis offset is added for clarity.

To clarify why the large fluorescence enhancement of zwitterionic MC molecules occurs near AuNS aggregates rather than near AuNTs, we explore the difference in the radiative decay rate enhancements between these two systems and assume $\frac{\gamma_r}{\gamma_{ro}} = k_r$. Since $k_r \propto \left|\mathbf{E}_p(\mathbf{r}_0)\right|^2$, we can further assume $k_r = \alpha_n A E_n^2$ (for the nth molecule near the plasmonic nanostructure), where α_n is a constant determined by the relative orientation of the nth molecule to the plasmonic nanostructure, E_n is the intensity of the enhanced E-field at the nth molecule, and A is a constant determined by the type of molecule. The fluorescence enhancement factor is obtained from the integrated fluorescence intensity of molecules at the AuNS aggregate (or AuNT) divided by that of the pure molecules, which is an average signal from the whole measured region. Accordingly, we compare the average emission rate enhancement: $\bar{k}_r = \frac{\sum \alpha_n A E_n^2}{m}$, where n is the number of molecules in all hot spots and m is the total number of molecules in the measured region. For the randomly distributed molecules (i.e., the effect of $\alpha_n A$ is negligible), the square of E-field intensity (E_n^2) increases by several orders of magnitude when n is much smaller than m, leading to an obvious fluorescence enhancement. Because the molecules located at the hot spots of AuNS aggregates and those of AuNTs only account for a small fraction of the total number of the molecules in the measured areas, our observation of fluorescence enhancement of zwitterionic MC molecules near AuNS aggregates rather than near AuNTs suggests that the E-field enhancement by the AuNS aggregates is larger than that by the AuNTs.

In fact, surface-enhanced Raman scattering (SERS) studies have demonstrated that the E-field enhancement by gap plasmonic modes at plasmonic NP aggregates can be significantly larger than that of single AuNTs.[50-54] Our FDTD simulations also show that the E-field of gap modes in the AuNS aggregate can be 50-60 times larger than that at single AuNTs (Figures 4a,b). This larger E-field enhancement at the interparticle gaps of the AuNS aggregate leads to a larger (250-360 times) emission rate enhancement of zwitterionic MC. Thus, we conclude that the large fluorescence enhancement arises from the large E-field at the AuNS aggregates. However, the large E-field cannot explain the observed photoswitchable fluorescence near the AuNS aggregates. To elucidate the physical principle of the photoswitchable fluorescence, we further explore the difference in fluorescence QY between zwitterionic MC and the quinoidal MC molecules near plasmonic nanostructures.

We assume that the MC molecule is a classic dipole and the non-radiative rate is determined by Ohmic loss in the environment:[9]

$$\gamma_{nr} \propto \frac{\gamma_0}{P_0} |\mathbf{E}_m|^2, \tag{6}$$

where γ_0 is the free-space decay rate, P_0 is the power emitted by the MC molecule, and $\mathbf{E}_m$ is the E-field emitted by the molecule. For our molecule-plasmon hybrid nanostructures, $\mathbf{E}_m$ equates $\mathbf{E}^0_m + \mathbf{E}_p(\mathbf{r}_0)$, where $\mathbf{E}^0_m$ is the E-field emitted by the molecule without plasmonic nanostructures. When $\mathbf{E}_p(\mathbf{r}_0)$ is much larger than $\mathbf{E}^0_m$, because $\gamma_0 = \frac{\gamma_{r0}}{\phi_0}$, we obtain:

$$\gamma_{nr} \propto \frac{\gamma_{r0}}{\phi_0 P_0} |\mathbf{E}_p(\mathbf{r}_0)|^2. \tag{7}$$

According to equations 6 and 7, we assume that the radiative rate and non-radiative rate of molecules near the AuNT be $\gamma_r = \alpha_n A E_n^2 \gamma_{r0}$ and $\gamma_{nr} = \beta_n B E_n^2 \frac{\gamma_{r0}}{\phi_0 P_0}$, respectively. β_n is a constant determined by the relative orientation of the nth molecule to the plasmonic nanostructure and B is a constant determined by the type of the molecule. E_n depends on the type of plasmonic nanostructures and the degree of the spectral overlap between the LSPRs

and the molecular fluorescence. We further denote $E_{1,n}$ as E_n for zwitterionic MC molecules near the AuNT, $E_{2,n}$ as E_n for zwitterionic MC molecules near the AuNS aggregate, $E_{3,n}$ as E_n for quinoidal MC molecules near the AuNT, and $E_{4,n}$ as E_n for quinoidal MC molecules near the AuNS aggregate.

Based on equations 1 and 2, we define the average QY of zwitterionic MC molecules near the AuNT ($\overline{\phi}_{AuNT}$) and near the AuNS aggregate ($\overline{\phi}_{Agg}$), and the average QY of quinoidal MC molecules near the AuNT ($\overline{\phi}'_{AuNT}$) and near the AuNS aggregate ($\overline{\phi}'_{Agg}$) as:

$$\overline{\phi}_{NT} = \frac{\overline{\alpha}_{NT}A\overline{E}_1^2\gamma_{r0}}{\overline{\alpha}_{NT}A\overline{E}_1^2\gamma_{r0} + \overline{\beta}_{NT}B\overline{E}_1^2\frac{\gamma_{r0}}{\phi_0 P_0} + \gamma_{ISC}}$$

$$= \frac{\overline{\alpha}_{NT}A}{\overline{\alpha}_{NT}A + \frac{\overline{\beta}_{NT}B}{\phi_0 P_0} + \frac{\gamma_{ISC}}{\overline{E}_1^2\gamma_{r0}}}, \tag{8}$$

$$\overline{\phi}_{Agg} = \frac{\overline{\alpha}_{Agg}A\overline{E}_2^2\gamma_{r0}}{\overline{\alpha}_{Agg}A\overline{E}_2^2\gamma_{r0} + \overline{\beta}_{Agg}B\overline{E}_2^2\frac{\gamma_{r0}}{\phi_0 P_0} + \gamma_{ISC}}$$

$$= \frac{\overline{\alpha}_{Agg}A}{\overline{\alpha}_{Agg}A + \frac{\overline{\beta}_{Agg}B}{\phi_0 P_0} + \frac{\gamma_{ISC}}{\overline{E}_2^2\gamma_{r0}}}, \tag{9}$$

$$\overline{\phi}'_{NT} = \frac{\overline{\alpha}_{NT}A'\overline{E}_3^2\gamma'_{r0}}{\overline{\alpha}_{NT}A'\overline{E}_3^2\gamma'_{r0} + \overline{\beta}_{NT}B'\overline{E}_3^2\frac{\gamma'_{r0}}{\phi'_0 P'_0}} = \frac{\overline{\alpha}_{NT}A'}{\overline{\alpha}_{NT}A' + \frac{\overline{\beta}_{NT}B'}{\phi'_0 P'_0}}, \tag{10}$$

and

$$\overline{\phi}'_{Agg} = \frac{\overline{\alpha}_{Agg}A'\overline{E}_4^2\gamma'_{r0}}{\overline{\alpha}_{Agg}A'\overline{E}_4^2\gamma'_{r0} + \overline{\beta}_{Agg}B'\overline{E}_4^2\frac{\gamma'_{r0}}{\phi'_0 P'_0}} = \frac{\overline{\alpha}_{Agg}A'}{\overline{\alpha}_{Agg}A' + \frac{\overline{\beta}_{Agg}B'}{\phi'_0 P'_0}}, \tag{11}$$

where $\bar{\alpha}_{NT}$ and $\bar{\beta}_{NT}$ are the average α and β of molecules near the AuNT; $\bar{\alpha}_{Agg}$ and $\bar{\beta}_{Agg}$ are

the average α and β of molecules near the AuNS aggregate; and $\bar{E}_1^2 = \frac{\sum E_{1,n}^2}{n}$, $\bar{E}_2^2 = \frac{\sum E_{2,n}^2}{n}$,

$\bar{E}_3^2 = \frac{\sum E_{3,n}^2}{n}$ and $\bar{E}_4^2 = \frac{\sum E_{4,n}^2}{n}$. Since no obvious enhancement or quenching was observed for

quinoidal MC molecules near the AuNT and AuNS aggregate, we assume $\bar{\phi}'_{AuNT} \approx \bar{\phi}'_{Agg} \approx$

ϕ'_0, which leads to $\bar{\alpha}_{NT} \approx \bar{\alpha}_{Agg}$ and $\bar{\beta}_{NT} \approx \bar{\beta}_{Agg}$. From equations 8 and 9, we know that, if

$\frac{\gamma_{ISC}}{\gamma_{ro}}$ is large, fluorescence QY can be significantly increased when the E-field is strongly

increased. This QY increase indicates that, even if the plasmon-induced non-radiative rate

enhancement is equivalent to the plasmon-induced radiative rate enhancement, a large

fluorescence enhancement can be still obtained due to the large ISC rate. Moreover, the

flourescence can be tuned by controlling the ISC rate.

We further investiged the fluorescence lifetime of zwitterionic MC molecules at single

AuNS aggregates. We employed fluorescence lifetime imaging microscopy (FLIM) to achieve

single-nanostruture resolution (see detailed information in Experimental Section).[38, 55] As a

control experiment, the FLIM image of MC-doped PMMA film without AuNSs is shown in

Figure 7a. The image was taken after UV irradiation of the film, which reveals that the

zwitterionic MC molecules in the PMMA film have a fluorescence lifetime of ~ 400 ps. The

FLIM image of MC-doped PMMA film that covers 60 nm AuNSs is shown in Figure 7b.

Most parts of the MC-doped PMMA film have a fluorescence lifetime of ~400 ps, while some

regions have a reduced fluorescence lifetime down to ~150 ps. The regions with shorter

lifetimes contain the AuNS aggregates, which are confirmed by SEM (Fig. 7b). Two

examples of the AuNS aggregrates are marked by black dashed rectangles in Figure 7b.

Figure 7c shows the dark-field optical microscopy image of the same sample covered with a

pure PMMA film. By comparing the dark-field optical image with the FLIM image, we

conclude that the fluorescence signals of reduced lifetime are obtained from the larger orange

spots with the stronger optical scattering in the dark-field optical image. In addition, green

spots with weaker scattering in the dark-field optical image are individual 60 nm AuNSs,

which have an LSPR peak wavelength around 545 nm (**Figure S7**). We verified the

individual AuNSs by an SEM image shown in the green dashed rectangle. No obvious

reduction of lifetime occurs at the green spots, meaning that the reduced fluorescence lifetime

of zwitterionic MC molecules at the aggregates arises from the strong E-field enhancement at

interparticle gaps. Since fluorescence lifetime is $-\tau = \frac{1}{\gamma_r}$, the lifetime measurements indicate

that the average k_r is less than 3. Since both γ_r and γ_{nr} increase with E-field enhancment,

equations 1 and 9 indicate that, without changes in γ_{ISC}, the fluorescence QY enhancement is

smaller than k_r. Therefore, the QY enhancement (as listed in Table 1) larger than k_r proves

that the ISC in zwitterionic MC molecules can further enhance the fluorescence when the E-

field enhancement is large.
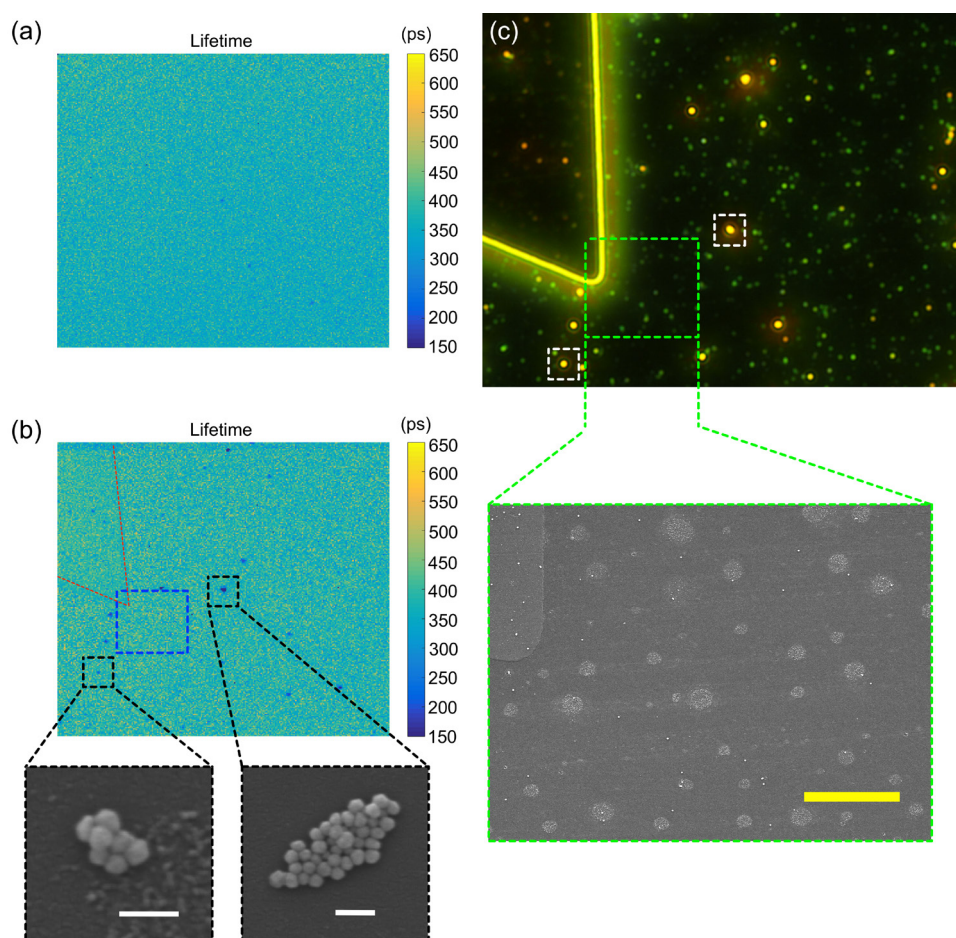
Figure 7. a) FLIM image of MC-doped PMMA without AuNSs after UV irradiation b) FLIM image of MC-doped PMMA with 60 nm AuNSs after UV irradiation. SEM images of AuNS aggregates obtained from the spots of the shorter lifetime in the black dashed rectangles. Red dashed lines outline the position of the marker. c) Dark-field optical image of the same area of the sample as shown in b). SEM image is obtained from the area indicated by the green dashed rectangle, which corresponds to the blue dashed rectangle in the FLIM image of b). The white dashed rectangles correspond to the black dashed rectangles in the FLIM image of b). The large circular regions with light color in the SEM image are residual PMMA on the glass substrate. White scale bars in SEM image of b) are 200 nm and yellow scale bar in SEM image of c) is 5 μm.

3. Conclusion

In summary, we elucidate how ISC influences the plasmon-enhanced fluorescence based on hybrid systems of plasmonic nanostructures and SP-derived MC molecules. Due to the high ISC rate, a large fluorescence enhancement can be obtained even if the plasmon-induced non-radiative rate enhancement is equivalent to the plasmon-induced radiative rate enhancement. The ISC-mediated fluorescence enhancement by the plasmonic nanostructures represents a new phenomenon in molecular plasmonics, which provides a new insight into how to select and design molecule-plasmon hybrid nanostructures to obtain a large plasmon-induced fluorescence enhancement. In addition, spiropyran and merocyanine molecules are sensitive to external stimuli and environmental changes, such as light with different wavelengths, temperature changes and pH changes. Therefore, we propose that ISC-mediated fluorescence enhancement can be used for applications such as optical modulators, optical switches, biosensing and bioimaging.[32, 39, 56-58]

4. Experimental Section

Sample preparation: Au nanospheres (AuNSs, Sigma Aldrich) with a diameter of 60 nm and Au nanotriangles (AuNTs) of variable sizes[37] were drop-coated on microscope calibration slides (AmScope) and dried naturally. Chlorobenzene (Fisher Scientific) was used to dissolve spiropyran (SP, Sigma-Aldrich) and PMMA (Sigma-Aldrich) with a weight ratio of 2:1 (SP:PMMA) to prepare PMMA films with a high concentration of SP molecules (8

19

wt%). A spin coater (Laurell Technologies) was employed to create SP-doped PMMA films on microscope slides with AuNSs or AuNTs. The spin coater was run with a speed of 2000 revolutions per minute for one minute.

Optical measurements: A dark-field optical microscope (Ti-E inverted microscope, Nikon) with a halogen white light source (12V, 100 W) was employed to measure the optical scattering spectra and the white-light-excited fluorescence of merocyanine (MC) molecules. A mercury light source (C-HGFIE, power: 130 W, Nikon) with excitation filters was used to generate UV light (DAPI Shift Filter set, excitation: 358 nm) and green light (TRITC HYQ Shift Filter set, excitation: 530-560 nm). The markers on microscope calibration slides were used to locate individual AuNS aggregates and AuNTs. The UV or green light (irradiation time was one minute) was applied to convert molecules from SP to MC isomers or from MC to SP isomers. We used an oil-immersion dark-field condenser in conjunction with 100× objective for single-particle and single-aggregate spectroscopy. Scanning electron microscopy (S5500, Hitachi) and transmission electron microscopy (JEM1400PLUS, JEOL) were used to measure the morphology of AuNS aggregates and AuNTs.

Temperature measurement: A thermometer was used to measure the temperature increase at the samples due to the photothermal effects. Upon irradiation with white light, the sample temperature increased from 22 °C to 31 °C within two minutes. The supply voltage of the white light source was 6 V. It should be noted that the thermometer was directly placed under the white light source and the head of thermometer is much larger than the irradiated spot in the dark-field optical measurement. Therefore, we believe that the actual temperature increase rate was faster than the measured value.

FDTD simulation: A commercially available software package (FDTD Solutions, Lumerical) was employed to conduct the finite-difference time-domain (FDTD) simulations. The AuNSs and AuNT were positioned at the top of a glass substrate (modeled with refractive index n=1.4). The refractive index of background environment was set as 1.49 to represent the

PMMA films. A plane wave was applied as the incident light source, and the scattered light was collected in transmission mode to obtain the optical scattering spectra. The wavelength-dependent dielectric functions of Au were adapted from Johnson and Christy.[59]

DFT simulation: Our density functional theory (DFT) and time-dependent density functional theory (TDDFT) calculations were performed using the Gaussian 09 suite of programs.[60] Semilocal (PBE[61])- and hybrid (B3LYP[62])-generalized gradient approximations were both considered. The 6-311G(d,p) and 6-311+G(2d,p) levels of theory were employed for configuration/total energy and vertical excitation calculations, respectively. The environment of the molecule within a PMMA matrix was simulated by applying a polarizable continuum model within integral equation formalism.[63]

Fluorescence lifetime imaging microscopy: A femtosecond titanium: sapphire laser tuned to 800 nm ($\approx$200 fs) (Mira 900, Coherent), galvo scanning mirrors (6215H, Cambridge Tech.), and a GaAsP photomultiplier tube (PMT) (H7422PA-40, Hamamatsu) in non-descanned detection scheme were utilized to constitute the FLIM setup. Before the signal reached the photon counting board (SPC-150, Becker and Hickl GmbH), a preamplifier (HFAC-26, Becker and Hickl GmbH) was used to ampilfy the output current of the PMT. The average laser power, TCSPC bin resolution, and FLIM pixel integration time were set to 4 mW, 20 ps, and 5 ms, respectively, when recording the fluorescence lifetime. A least squares method using a model of a single exponential decay was then used to fit the fluorescence lifetime.[64]

Supporting Information
Supporting Information is available from the Wiley Online Library or from the author.

References

[1] S. Noda, M. Fujita, T. Asano, *Nat. Photon.* **2007**, 1, 449.

[2] J. R. Lakowicz, *Anal. Biochem.* **2005**, 337, 171.

[3] M. Pelton, *Nat. Photon.* **2015**, 9, 427.

[4] H. Cang, Y. Liu, Y. Wang, X. Yin, X. Zhang, *Nano Lett.* **2013**, 13, 5949.

[5] P. Lodahl, A. Floris van Driel, I. S. Nikolaev, A. Irman, K. Overgaag, D. Vanmaekelbergh, W. L. Vos, *Nature* **2004**, 430, 654.

[6] J.-H. Song, T. Atay, S. Shi, H. Urabe, A. V. Nurmikko, *Nano Lett.* **2005**, 5, 1557.

[7] C. Belacel, B. Habert, F. Bigourdan, F. Marquier, J. P. Hugonin, S. Michaelis de Vasconcellos, X. Lafosse, L. Coolen, C. Schwob, C. Javaux, B. Dubertret, J. J. Greffet, P. Senellart, A. Maitre, *Nano Lett.* **2013**, 13, 1516.

[8] E. M. Purcell, H. C. Torrey, R. V. Pound, *Phys. Rev.* **1946**, 69, 37.

[9] P. Anger, P. Bharadwaj, L. Novotny, *Phys. Rev. Lett.* **2006**, 96, 113002.

[10] S. Kühn, U. Håkanson, L. Rogobete, V. Sandoghdar, *Phys. Rev. Lett.* **2006**, 97, 017402.

[11] G. M. Akselrod, C. Argyropoulos, T. B. Hoang, C. Ciracì, C. Fang, J. Huang, D. R. Smith, M. H. Mikkelsen, *Nat. Photon.* **2014**, 8, 835.

[12] A. Rose, T. B. Hoang, F. McGuire, J. J. Mock, C. Ciracì, D. R. Smith, M. H. Mikkelsen, *Nano Lett.* **2014**, 14, 4797.

[13] O. G. Tovmachenko, C. Graf, D. J. van den Heuvel, A. van Blaaderen, H. C. Gerritsen, *Adv. Mater.* **2006**, 18, 91.

[14] R. Bardhan, N. K. Grady, J. R. Cole, A. Joshi, N. J. Halas, *ACS Nano* **2009**, 3, 744.

[15] M. Fujita, S. Takahashi, Y. Tanaka, T. Asano, S. Noda, *Science* **2005**, 308, 1296.

[16] H. Chen, L. Shao, Q. Li, J. Wang, *Chem. Soc. Rev.* **2013**, 42, 2679.

[17] S. Eustis, M. A. El-Sayed, *Chem. Soc. Rev.* **2006**, 35, 209.

[18] N. J. Halas, S. Lal, W.-S. Chang, S. Link, P. Nordlander, *Chem. Rev.* **2011**, 111, 3913.

[19] T. Ming, H. Chen, R. Jiang, Q. Li, J. Wang, *J. Phys. Chem. Lett.* **2012**, 3, 191.

[20] N. Gandra, C. Portz, L. Tian, R. Tang, B. Xu, S. Achilefu, S. Singamaneni, *Angew. Chem. Int. Ed.* **2014**, 53, 866.

[21] C. Ayala-Orozco, J. G. Liu, M. W. Knight, Y. Wang, J. K. Day, P. Nordlander, N. J. Halas, *Nano Lett.* **2014**, 14, 2926.

[22] F. Tam, G. P. Goodrich, B. R. Johnson, N. J. Halas, *Nano Lett.* **2007**, 7, 496.

[23] V. Giannini, A. I. Fernández-Domínguez, S. C. Heck, S. A. Maier, *Chem. Rev.* **2011**, 111, 3888.

[24] Y. Gu, L. Wang, P. Ren, J. Zhang, T. Zhang, O. J. F. Martin, Q. Gong, *Nano Lett.* **2012**, 12, 2488.

[25] T. Ming, L. Zhao, H. Chen, K. C. Woo, J. Wang, H.-Q. Lin, *Nano Lett.* **2011**, 11, 2296.

[26] P. Holzmeister, E. Pibiri, J. J. Schmied, T. Sen, G. P. Acuna, P. Tinnefeld, *Nat. Commun.* **2014**, 5.

[27] Y. Fu, J. Zhang, J. R. Lakowicz, *J. Am. Chem. Soc.* **2010**, 132, 5540.

[28] T. Ming, L. Zhao, Z. Yang, H. Chen, L. Sun, J. Wang, C. Yan, *Nano Lett.* **2009**, 9, 3896.

[29] A. Kinkhabwala, Z. Yu, S. Fan, Y. Avlasevich, K. Mullen, W. E. Moerner, *Nat. Photon.* **2009**, 3, 654.

[30] H. Gorner, *Phys. Chem. Chem. Phys.* **2001**, 3, 416.

[31] A. K. Chibisov, H. Görner, *J. Photochem. Photobiol. A* **1997**, 105, 261.

[32] R. Klajn, *Chem. Soc. Rev.* **2014**, 43, 148.

[33] T. Ming, L. Zhao, M. Xiao, J. Wang, *Small* **2010**, 6, 2514.

[34] F. Kita, W. Adam, P. Jordan, W. M. Nau, J. Wirz, *J. Am. Chem. Soc.* **1999**, 121, 9265.

[35] S. Cogan, Y. Haas, S. Zilberg, *J. Photochem. Photobiol. A* **2007**, 190, 200.

[36] L. Salem, C. Rowland, *Angew. Chem. Int. Ed. in English* **1972**, 11, 92.

[37] L. Scarabelli, M. Coronado-Puchau, J. J. Giner-Casares, J. Langer, L. M. Liz-Marzán, *ACS Nano* **2014**, 8, 5833.

[38] M. Wang, B. Bangalore Rajeeva, L. Scarabelli, E. P. Perillo, A. K. Dunn, L. M. Liz-Marzán, Y. Zheng, *J. Phys. Chem. C* **2016**, 120, 14820.

[39] M.-Q. Zhu, L. Zhu, J. J. Han, W. Wu, J. K. Hurst, A. D. Q. Li, *J. Am. Chem. Soc.* **2006**, 128, 4303.

[40] Y. Xue, J. Tian, W. Tian, P. Gong, J. Dai, X. Wang, *J. Phys. Chem. C* **2015**, 119, 20762.

[41] W. Tian, J. Tian, *Langmuir* **2014**, 30, 3223.

[42] X. Song, J. Zhou, Y. Li, Y. Tang, *J. Photochem. Photobiol. A* **1995**, 92, 99.

[43] Y. Wu, T. Sasaki, K. Kazushi, T. Seo, K. Sakurai, *J. Phys. Chem. B* **2008**, 112, 7530.

[44] R. Rosario, D. Gust, M. Hayes, J. Springer, A. A. Garcia, *Langmuir* **2003**, 19, 8801.

[45] J. T. C. Wojtyk, A. Wasey, P. M. Kazmaier, S. Hoz, E. Buncel, *J. Phys. Chem. A* **2000**, 104, 9046.

[46] P. Bharadwaj, L. Novotny, *Opt. Express* **2007**, 15, 14266.

[47] Y. Xiong, J. M. McLellan, J. Chen, Y. Yin, Z.-Y. Li, Y. Xia, *J. Am. Chem. Soc.* **2005**, 127, 17118.

[48] M. Rycenga, P. H. C. Camargo, W. Li, C. H. Moran, Y. Xia, *J. Phys. Chem. Lett.* **2010**, 1, 696.

[49] Y. Sun, Y. Xia, *Science* **2002**, 298, 2176.

[50] K. L. Wustholz, A.-I. Henry, J. M. McMahon, R. G. Freeman, N. Valley, M. E. Piotti, M. J. Natan, G. C. Schatz, R. P. V. Duyne, *J. Am. Chem. Soc.* **2010**, 132, 10903.

[51] S. L. Kleinman, B. Sharma, M. G. Blaber, A.-I. Henry, N. Valley, R. G. Freeman, M. J. Natan, G. C. Schatz, R. P. Van Duyne, *J. Am. Chem. Soc.* **2013**, 135, 301.

[52] S. L. Kleinman, R. R. Frontiera, A.-I. Henry, J. A. Dieringer, R. P. Van Duyne, *Phys. Chem. Chem. Phys.* **2013**, 15, 21.

[53] J. P. Camden, J. A. Dieringer, Y. Wang, D. J. Masiello, L. D. Marks, G. C. Schatz, R. P. Van Duyne, *J. Am. Chem. Soc.* **2008**, 130, 12616.

[54] N. Pazos-Perez, C. S. Wagner, J. M. Romo-Herrera, L. M. Liz-Marzán, F. J. García de Abajo, A. Wittemann, A. Fery, R. A. Alvarez-Puebla, *Angew. Chem. Int. Ed.* **2012**, 51, 12688.

[55] E. P. Perillo, Y.-L. Liu, K. Huynh, C. Liu, C.-K. Chou, M.-C. Hung, H.-C. Yeh, A. K. Dunn, *Nat. Commun.* **2015**, 6.

[56] M.-Q. Zhu, G.-F. Zhang, C. Li, M. P. Aldred, E. Chang, R. A. Drezek, A. D. Q. Li, *J. Am. Chem. Soc.* **2011**, 133, 365.

[57] M.-Q. Zhu, G.-F. Zhang, Z. Hu, M. P. Aldred, C. Li, W.-L. Gong, T. Chen, Z.-L. Huang, S. Liu, *Macromolecules* **2014**, 47, 1543.

[58] G. Berkovic, V. Krongauz, V. Weiss, *Chem. Rev.* **2000**, 100, 1741.

[59] P. B. Johnson, R. W. Christy, *Phys. Rev. B* **1972**, 6, 4370.

[60] G. W. T. M. J. Frisch, H. B. Schlegel, G. E. Scuseria, M. A. Robb, J. R. Cheeseman, G. Scalmani, V. Barone, B. Mennucci, G. A. Petersson, H. Nakatsuji, M. Caricato, X. Li, H. P. Hratchian, A. F. Izmaylov, J. Bloino, G. Zheng, J. L. Sonnenberg, M. Hada, M. Ehara, K. Toyota, R. Fukuda, J. Hasegawa, M. Ishida, T. Nakajima, Y. Honda, O. Kitao, H. Nakai, T. Vreven, J.A.Montgomery,J. E. Peralta,F.Ogliaro, M. Bearpark,J.J.Heyd, E. Brothers,K.N.Kudin, V.N. Staroverov, T. Keith, R. Kobayashi, J. Normald, K. Raghavachari, A. Rendell, J. C. Burant,S.S.Iyengar, J. Tomasi, M. Cossi,N.Rega, J. M. Millam, M. Klene, J. E. Knox, J. B. Cross, V. Bakken, C. Adamo, J. Jaramillo,R.Gomperts,R. E.Stratmann,O. Yazyev,A.J.Austin, R. Cammi, C. Pomelli, J. W. Ochterski, R. L. Martin, K. Morokuma,V. G. Zakrzewski, G. A.

Voth,P.Salvador, J. J. Dannenberg,S.Dapprich, A. D. Daniels, O. Farkas,J.B. Foresman,J.V.Ortiz, J.Cioslowskiand, D. J. Fox, Gaussian 09 Revis. C.01, Gaussian, Inc., Wallingord CT, 2010.

[61]   J. P. Perdew, K. Burke, M. Ernzerhof, *Phys. Rev. Lett.* **1996**, 77, 3865.

[62]   A. D. Becke, *J. Chem. Phys.* **1993**, 98, 5648.

[63]   B. Mennucci, E. Cancès, J. Tomasi, *J. Phys. Chem. B* **1997**, 101, 10506.

[64]   A. M. Sean C. Warren, Dominic Alibhai, Douglas J. Kelly, Clifford Talbot, Yuriy Alexandrov, Ian Munro, Matilda Katan, Chris Dunsby, Paul M. W. French *PLOS ONE* **2013**, 8, e70687.